The Astrophysical Journal, 897:31 (13pp), 2020 July 1 https://doi.org/10.3847/1538-4357/ab93c1

The Inner Disk of RY Tau: Evidence of Stellar Occultation by the Disk Atmosphere at the Sublimation Rim from *K*-band Continuum Interferometry

Claire L. Davies[1], Stefan Kraus[1], Tim J. Harries[1], John D. Monnier[2], Brian Kloppenborg[3], Alicia Aarnio[4], Fabien Baron[3], Rebeca Garcia Lopez[5], Rafael Millan-Gabet[6], Robert Parks[3], Ettore Pedretti[7], Karine Perraut[8], Judit Sturmann[9], Laszlo Sturmann[9], Theo A. ten Brummelaar[9], and Yamina Touhami[3]
[1] Astrophysics Group, School of Physics, University of Exeter, Stocker Road, Exeter, EX4 4QL, UK; c.davies3@exeter.ac.uk
[2] Department of Astronomy, University of Michigan, Ann Arbor, MI 48109, USA
[3] Department of Physics and Astronomy, Georgia State University, Atlanta, GA 30302, USA
[4] University of Colorado Boulder, Boulder, CO 80303, USA
[5] School of Physics, University College Dublin, Belfield, Dublin 4, Ireland
[6] Infrared Processing and Analysis Center, California Institute of Technology, Pasadena, CA 91125, USA
[7] STFC Rutherford Appleton Laboratory, Harwell Science & Innovation Campus, OX11 0QX, UK
[8] Univ. Grenoble Alpes, CNRS, IPAG, F-38000 Grenoble, France
[9] The CHARA Array of Georgia State University, Mount Wilson Observatory, Mount Wilson, CA 91203, USA
Received 2020 March 16; revised 2020 May 6; accepted 2020 May 14; published 2020 June 30

Abstract

We present models of the inner region of the circumstellar disk of RY Tau that aim to explain our near-infrared (*K*-band: 2.1 μm) interferometric observations, while remaining consistent with the optical to near-infrared portions of the spectral energy distribution. Our submilliarcsecond-resolution CHARA Array observations are supplemented with shorter baseline, archival data from PTI, KI, and VLTI/GRAVITY and modeled using an axisymmetric Monte Carlo radiative transfer code. The *K*-band visibilities are well fit by models incorporating a central star illuminating a disk with an inner edge shaped by dust sublimation at 0.210 ± 0.005 au, assuming a viewing geometry adopted from millimeter interferometry (65° inclined with a disk major axis position angle of 23°). This sublimation radius is consistent with that expected of silicate grains with a maximum size of 0.36–0.40 μm contributing to the opacity, and is an order of magnitude further from the star than the theoretical magnetospheric truncation radius. The visibilities on the longest baselines probed by CHARA indicate that we lack a clear line of sight to the stellar photosphere. Instead, our analysis shows that the central star is occulted by the disk surface layers close to the sublimation rim. While we do not see direct evidence of temporal variability in our multiepoch CHARA observations, we suggest the aperiodic photometric variability of RY Tau is likely related temporal and/or azimuthal variations in the structure of the disk surface layers.

Unified Astronomy Thesaurus concepts: Optical interferometry (1168); Star formation (1569); Circumstellar disks (235); Young stellar objects (1834); T Tauri stars (1681); Herbig Ae/Be stars (723); Infrared excess (788); Near infrared astronomy (1093); Radiative transfer (1335)

1. Introduction

The reprocessing of starlight by dust in the innermost regions of the disks of young stellar objects (YSOs) produces strong near-infrared (NIR) continuum emission in excess of that expected from purely photospheric emission. The milliarcsecond (mas) and submas resolution provided by NIR interferometry at ~1–3 μm can be used to spatially resolve this region and help to explain the shape and structure of the environments in which planets form and evolve. The earliest NIR interferometric studies of disks showed that dust had a finite inner limit and did not extend down to the stellar surface (Millan-Gabet et al. 1999; Akeson et al. 2000). The location of this inner edge is likely forged by dust sublimation (Tuthill et al. 2001; Monnier & Millan-Gabet 2002) with the slope of the inner edge size–stellar luminosity relation indicating a dust sublimation temperature, $T_{\rm sub} \sim 1800$ K (Lazareff et al. 2017; Gravity Collaboration et al. 2019).

The lack of any strong viewing-angle dependency to the closure phase signals, $\phi_{\rm CP}$, obtained via NIR interferometry further indicated that this sublimation rim was likely a curved surface rather than a vertical wall (Monnier et al. 2005). This curvature arises naturally, due to the dependence of $T_{\rm sub}$ and the grain cooling efficiency on the gas density; the size distribution of dust grains; the preferential settling of larger grains toward the disk midplane; and the relative abundance of different grain compositions (Pollack et al. 1994; Isella & Natta 2005; Tannirkulam et al. 2007; Kama et al. 2009; McClure et al. 2013).

Herein, we focus on RY Tau (spectral type G1, Calvet et al. 2004) and study the shape and structure of its circumstellar NIR-emitting region. The existence of circumstellar material around RY Tau was first identified through its strong infrared (IR) excess (Mendoza 1968). Analysis of RY Tau 's spectral energy distribution (SED) across IR wavelengths led to its classification as a pretransitional disk (Marsh & Mahoney 1992; Furlan et al. 2009; Espaillat et al. 2011): the NIR excess is typical of accretion disks, but the relative dearth of mid-IR (MIR) excess flux indicates the likely presence of a dust cavity or optically thin region of the disk. A dust cavity was indeed observed via high-resolution millimeter (mm) imaging obtained with the Combined Array for Research in Millimeter-wave Astronomy (CARMA; Isella et al. 2010) and the Atacama Large Millimeter Array (ALMA; Long et al. 2018, 2019). The object's microjet emission, observed at optical (St-Onge & Bastien 2008) and NIR wavelengths (Garufi et al. 2019), and its relatively strong mass accretion rate, (typical of disks with substantial mass reservoirs in their innermost disk regions; Calvet et al. 2004; Mendigutía et al. 2011) also support this classification.

Table 1
CHARA Observation Log

Date (UT)	Beam Combiner	Stations	Calibrator(s)
2009 Oct 31	CLASSIC	E1 S1	1
2009 Nov 1	CLASSIC	E1 S1	2
2009 Nov 24	CLASSIC	S1 W1	3
2010 Sep 29	CLIMB	S1 E1 W1	2, 4
2010 Oct 2	CLIMB	S1 E1 W1	2, 4
2010 Oct 4	CLIMB	S1 E1 W1	2, 4
2010 Dec 2	CLIMB	S2 E1 W2	1, 2
2011 Oct 27	CLIMB	S2 E2 W2	2
2011 Dec 22	CLIMB	S2 E2 W1	2, 5
2012 Nov 26	CLIMB	S1 E1 W1	2, 6
2012 Nov 27	CLIMB	S1 E1 W1	2

Note. Calibrators and their UD diameters in mas: 1: HD 32480 (0.221 ± 0.016); 2: HD 24365 (0.317 ± 0.022); 3: HD 28447 (0.503 ± 0.035); 4: HD 25461 (0.245 ± 0.017); 5: HD 30912 (0.44 ± 0.10); 6: HD 33252 (0.299 ± 0.021).

Direct observation of the inner tens of au of the disk has remained difficult. Hubble Space Telescope (HST; Agra-Amboage et al. 2009) and polarized intensity images obtained in the optical and NIR with Very Large Telescope (VLT)/SPHERE (Garufi et al. 2019) and Subaru/HiCIAO (Takami et al. 2013) are dominated by an optically thin scattering layer above the disk surface. The astrophysical nature of this scattering surface remains unclear with a remnant spherical envelope or a dusty outflow caused by a magnetospheric or photoevaporative wind providing possible explanations.

NIR and MIR interferometric observations of RY Tau—obtained with the Palomar Testbed Interferometer (PTI; Akeson et al. 2005), the Infrared Optical Telescope Array (IOTA; Monnier et al. 2005) and the Very Large telescope Interferometer's MID-infrared Interferometer instrument (VLTI/MIDI; Schegerer et al. 2008)—have previously probed the circumstellar emission on subau to au scales. However, these observations have been limited by (i) the $\lesssim$100 m maximum baseline lengths of the interferometric arrays; (ii) the poor baseline position angle, PA_b, coverage of the observations; (iii) poor constraints on the exact circumstellar-versus-stellar flux contribution, due to the intrinsically variable nature of RY Tau. Akeson et al. (2005) and Monnier et al. (2006) attempted to estimate the characteristic size of the NIR-emitting region, with model-dependent estimates of $\sim$0.2–0.6 au (using a stellar distance, $d = 140$ pc), broadly consistent with the expected dust sublimation radius, $R_{\rm sub}$, given the object's luminosity ($\sim$6–12 $L_\odot$, e.g., Calvet et al. 2004; Garufi et al. 2019; Long et al. 2019).

In these prior NIR and MIR interferometric studies, the disk inclination, $i_{\rm d}$, was either assumed to be face-on (i.e., $i_{\rm d} = 0°$, Monnier et al. 2006; Schegerer et al. 2008), or left free in the fitting and loosely constrained around $i_{\rm d} \approx 20°$–$25°$ (Akeson et al. 2005). This is in stark contrast to the highly inclined ($i_{\rm d} \sim 60°$–$70°$) disk observed by CARMA (Isella et al. 2010) and ALMA (Long et al. 2018, 2019; Pinilla et al. 2018). A more highly inclined inner disk is also supported by the nature of the optical and IR photometric variability exhibited by RY Tau, which is likely to arise due to line of sight occultation of the stellar photosphere by circumstellar material (Grankin et al. 2007; Petrov et al. 2019).

This study continues our analysis of YSOs observed with the Center for High Angular Resolution Astronomy (CHARA) Array's two-telescope (CLASSIC) and three-telescope (CLIMB) combiners (see Davies et al. 2018; Setterholm et al. 2018; Labdon et al. 2019). A description of our *K*-band observations of RY Tau with CLASSIC and CLIMB is presented in Section 2.1. The $\sim$330 m maximum baselines of the CHARA Array provide us with unrivaled spatial resolution in the NIR. We supplement our CLASSIC and CLIMB observations with archival short-baseline *K*-band interferometric data (Section 2.2), thus benefiting from a greatly improved PA_b coverage compared with the Akeson et al. (2005) and Monnier et al. (2005) studies. We build on work conducted by Tannirkulam et al. (2008), Davies et al. (2018), and Labdon et al. (2019), and use the TORUS Monte Carlo radiative transfer code (Harries et al. 2019) to explore the shape and structure of the NIR circumstellar emission component. We provide details of our modeling and results in Section 3, and present a discussion of our results in Section 4.

2. Observations and Supplementary Archival Data

2.1. CHARA Interferometry

The CLASSIC and CLIMB beam combiners (ten Brummelaar et al. 2013) of the CHARA Array were used to obtain *K*-band interferometric observations of RY Tau between 2009 October and 2012 November. The CHARA Array is Y-shaped and comprises six 1 m class telescopes located at Mount Wilson Observatory with operational baselines of 34–331 m (corresponding to a maximum resolution[10] of 0.66 mas, ten Brummelaar et al. 2005). A log of our observations is presented in Table 1. The (u, v)-plane coverage is displayed by the red and blue data points in Figure 1.

The data were reduced using a pipeline developed at the University of Michigan, which is better suited to recovering faint fringes for low-visibility data than the standard CHARA reduction pipeline of ten Brummelaar et al. (2012). Further details regarding the reduction procedure are given in Davies et al. (2018). Calibrator stars were observed before and/or after each observation and used to calibrate the squared visibilities and $\phi_{\rm CP}$. None of the calibrators used are known members of binary or multiple systems. Where CLIMB data was obtained for a calibrator, the $\phi_{\rm CP}$ were inspected as a further check for binarity. No evidence for the presence of companions (non-zero $\phi_{\rm CP}$) were found. Calibrator uniform disk (UD) diameters, retrieved from JMMC SearchCal (Bonneau et al. 2006, 2011), when available, or from getCal,[11] (see Table 1), were used to calculate the transfer function and are listed in the footnote to Table 1. The calibrated data will be made accessible in OIFITS format (Pauls et al. 2005; Duvert et al. 2017) through the Optical interferometry Database (OiDb; Haubois et al. 2014) of the JMMC and through the CHARA archive (J. Jones et al. 2020, in preparation), hosted by Georgia State University, following publication.

2.2. Complementary Short-baseline Interferometry

To probe more extended components of the circumstellar emission from RY Tau, we supplemented our CHARA observations with shorter baseline, *K*-band archival interferometric observations (see Table 2). Calibrated PTI (Colavita et al. 1999)

[10] $\lambda/2B$ with λ the operational wavelength (2.13 μm) and B the separation between telescopes.
[11] http://nexsci.caltech.edu/software/getCal/

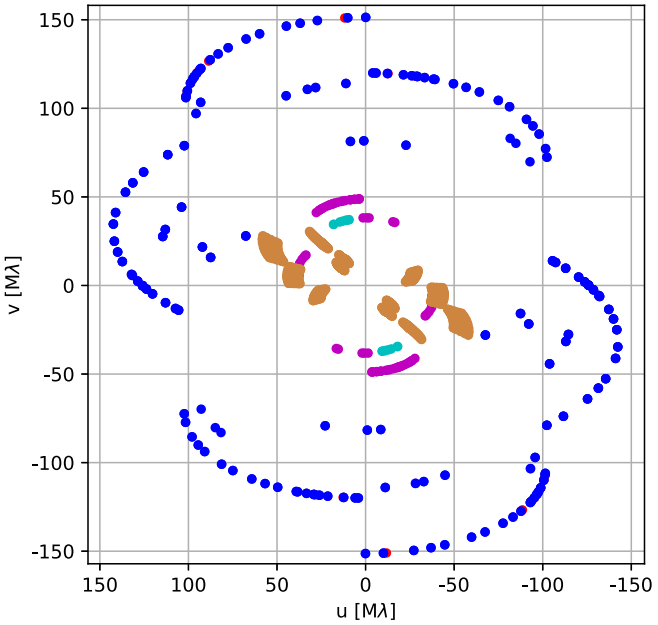

Figure 1. (u, v)-plane coverage of the compiled K-band interferometry. North is up; east is left. CLASSIC and CLIMB observations (see Table 1) are indicated by red and blue data points, respectively. The supplementary short-baseline interferometric data from KI (cyan), PTI (magenta), and VLTI/GRAVITY (orange; see Table 2) are also shown.

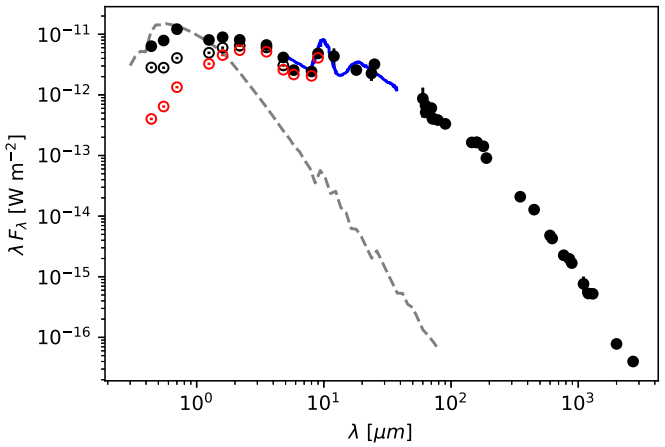

Figure 2. Comparison of our compiled SED for RY Tau (see Section 3.1.1 and Appendix A for details) with the spectrum of a star with properties given in Table 3 (gray dashed line). Red and black open circles represent the "faint" epoch photometry from Petrov et al. (2019), with $A_V = 0$ (i.e., no dereddening applied) and $A_V = 1.6$, respectively. Black filled circles represent the "bright" epoch photometry from Petrov et al. (2019) with $A_V = 1.6$. The blue line represents the Spitzer spectrum.

data, originally published in Akeson et al. (2005), were provided by Rachel Akeson while reduced Keck Interferometer (KI; Colavita et al. 2013) data were retrieved from the Keck Observatory Archive. The wide-band KI data were calibrated using the NExScI Wide-band Interferometric Visibility Calibration (wbCalib v1.4.4) tool with the flux bias correction and ratio correction options selected.

Data obtained using the GRAVITY instrument (Gravity Collaboration et al. 2017) of the VLTI were also retrieved from the European Southern Observatory archive. The data were reduced and calibrated using GRAVITY pipeline, version 1.1.2, with default settings. We restrict our analysis to the low spectral dispersion ($R \sim 30$) GRAVITY fringe tracker data which provides five wavelength channels across the K band. We exclude the first spectral channel from our analysis, as these are systematically lower than the other channels (likely due to corruption by the metrology laser which operates at $\lambda = 1.08$ μm). The calibrators (and their UDs) used to calibrate the KI and VLTI/GRAVITY data are provided in the footnote to Table 2.

Table 2
Supplementary Interferometric Data

Date (UT)	Program ID	Stations	Calibrator(s)
	PTI		
2001 Sep 24	⋯	NW	⋯
2001 Sep 27	⋯	NW	⋯
2001 Oct 3	⋯	NS	⋯
2001 Oct 17	⋯	NW	⋯
2001 Nov 7	⋯	NS	⋯
2001 Nov 17	⋯	NS	⋯
2001 Nov 22	⋯	NS	⋯
2003 Oct 14	⋯	SW	⋯
2003 Oct 15	⋯	SW	⋯
	KI		
2006 Nov 12	32	K1K2	1, 2
2008 Dec 15	48	K1K2	3
2010 Nov 24	51	K1K2	1
	VLTI/GRAVITY		
2017 Dec 10	0100.C-0278	UT1-UT2-UT3-UT4	4, 5

Note. Calibrators are listed in column 4 when data were (re)reduced. Their identifiers (and UD diameters in mas) are 1: HD 27777 (0.17 ± 0.01); 2: HD 31592 (0.19 ± 0.01); 3: HD 283934 (0.071 ± 0.014); 4: HD 58923 (0.433 ± 0.002); 5: HD 96113 (0.367 ± 0.001).

2.3. Multiband Photometry and MIR Spectroscopy

Multiwavelength photometry for RY Tau was retrieved from the literature. These data were primarily acquired as an additional assessment of the NIR flux provided by our models. This is vital, as visibility modeling is known to be affected by degeneracies between the stellar-to-circumstellar flux contrast and the characteristic size of the emitting region (e.g., Lazareff et al. 2017). The collated data is presented in Appendix A and shown in Figure 2, compared with the Kurucz (1979) spectrum of a star with effective temperature, $T_{\rm eff} = 5945$ K, luminosity, $L_\star = 11.6\ L_\odot$, and surface gravity, $\log(g) = 3.8$ (see Table 3). The strong IR excess arising from the presence of circumstellar material is clearly visible.

As RY Tau is variable across optical and NIR wavelengths (e.g., Grankin et al. 2007; Petrov et al. 2019), two sets of Johnson-*BVRJHKLM* photometry are tabulated in Appendix A and shown in Figure 2. These are taken from the Petrov et al. (2019) photometric monitoring study, and are characteristic of a "bright" (black filled circles) and a "faint" (red and black open circles) epoch, obtained on 1989 October 25 and 2016 November 11, respectively. The red open circles have not been dereddened (i.e., assumes interstellar extinction, $A_V = 0.0$), while the black open and filled circles have been dereddened using $A_V = 1.6$ (see Table 3). As our interferometric data were

Table 3
Stellar Parameters

	$T_{\rm eff}$ (K)	log g	d (pc)	A_V	$L_\star$ ($L_\odot$)	$R_\star$ ($R_\odot$)	$M_\star$ ($M_\odot$)
Herein	5945	3.8	140	1.6	11.6	3.2	2.0
L19	6220	4.0	128	1.94	12.3	2.37	2.04
G19	5750	3.58	133	1.5	6.3	3.7	≈1.9

Note. For the "Herein" row, $T_{\rm eff}$, $M_\star$, and log g are from Calvet et al. (2004); d from Kenyon et al. (1994), Galli et al. (2018); and A_V from Petrov et al. (2019). See the text for details regarding the calculation of $L_\star$ and $R_\star$. Radii from L19 and G19 were calculated using log g and $M_\star$.

obtained over several years, and the photometry was not obtained contemporaneously with the interferometry, we adopt the red and black filled data as indicators of the upper and lower bounds to the optical and NIR flux allowed in our models.

A postprocessed, flux-calibrated Spitzer Infrared Spectrograph (IRS; Houck et al. 2004) spectrum for RY Tau (Lebouteiller et al. 2011, AORkey 27185920) was retrieved from the Cornell Atlas of Spitzer/IRS Sources (CASSIS[12] version 7). This is shown by the blue line in Figure 2.

3. Modeling and Results

The new and archival visibilities and $\phi_{\rm CP}$ obtained for RY Tau are displayed in Figure 3. Visibilities are plotted with respect to the deprojected baseline length, $B_{\rm eff}$, calculated from the baseline vectors using $i_{\rm d} = 65°$, and a disk minor axis position angle, $\rm PA_{minor} = 113°$ (see Section 3.2 for details regarding the adopted disk geometry), following

$$B_{\rm eff} = B[\sin^2(\phi) + \cos^2(i)\cos^2(\phi)]^{1/2}\,. \quad (1)$$

Here, ϕ is the difference between $\rm PA_b$ and $\rm PA_{minor}$. Using $B_{\rm eff}$ rather than the true baseline length, B, accounts for the fact that the brightness distribution along $\rm PA_b$, which traces $\rm PA_{minor}$, is foreshortened in comparison with that along $\rm PA_b$, which traces the disk major axis position angle, $\rm PA_{major}$.

Before undertaking detailed modeling, we visually inspected the data for signs of temporal variations in the underlying brightness distribution. Specifically, we inspected the vertical spread in visibility with respect to $B_{\rm eff}$ (top panel of Figure 3). The vertical spread in visibility with $B_{\rm eff}$ across the GRAVITY data (orange data points) is dominated by the spectral dependence: the longer wavelength spectral channels display shallower visibility profiles. This effect is consistent with the idea that longer wavelengths probe comparatively cooler regions of the circumstellar disk, which are more extended and thus more resolved. In comparison, our CLIMB and CLASSIC data (blue and red data points, respectively) are all obtained using the same filter with no spectral dispersion, so spectral variations cannot explain the vertical spread in these data. Splitting the CLIMB data up by observation date does not reveal noticeable temporal variations in the visibility. Instead, a similar level of vertical spread in visibility to that in the top panel of Figure 3 is present at each observational epoch. We also see no dependence of the CLIMB and CLASSIC visibilities on $\rm PA_b$, although we note that our (u, v)-plane

[12] The Cornell Atlas of Spitzer/IRS Sources (CASSIS) is a product of the Infrared Science Center at Cornell University, supported by NASA and JPL.

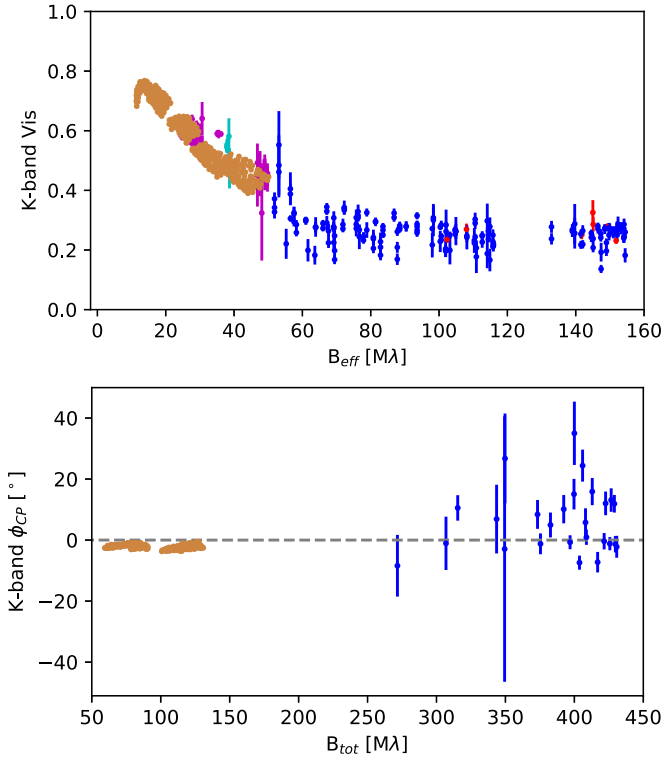

Figure 3. Observed visibilities (top) and $\phi_{\rm CP}$ (bottom). Visibilities are plotted with respect to the deprojected baseline length, assuming $i_{\rm d} = 65°$ and $\rm PA_{major} = 23°$ (see Equation (1)). Individual data points are color coded as in Figure 1.

coverage does not directly probe the ∼10°–15° region around $\rm PA_{minor}$ (see Figure 1). The vertical spread in the CLIMB and CLASSIC data is more likely associated with measurement uncertainty and/or an underestimation of calibration uncertainties rather than an underlying astrophysical process. Thus, we adopt an additional 10% systematic uncertainty on the CHARA data.

A similar assessment of the potential effect of temporal variability on the $\phi_{\rm CP}$ measurements (shown in the bottom panel of Figure 3) was not possible due to (i) the sparsity of CLIMB data from individual nights and (ii) the availability of only a single epoch of GRAVITY data for comparison. Consequently, we are unable to reliably assess the cause of our non-zero CLIMB $\phi_{\rm CP}$ measurements.

3.1. Monte Carlo Radiative Transfer Models

We model RY Tau as a centrally illuminated passive disk using the TORUS Monte Carlo radiative transfer code (Harries 2000; Tannirkulam et al. 2007; Harries et al. 2019). In this scenario, viscous heating due to accretion is assumed to be minimal, and the central star is the only source of heating. The Lucy (1999) algorithm is used to compute radiative equilibrium on a two-dimensional, cylindrical adaptive mesh grid.

Polarized intensity images of RY Tau have previously highlighted a notable scattered-light contribution across optical and NIR wavelengths (Takami et al. 2013; Garufi et al. 2019). The distance scales probed by our interferometric observations are much more compact, and we anticipated the scattered-light contribution to cause the visibilities to deviate from a value of 1.0 at the shortest baseline lengths. From the top panel of

Figure 3, it is difficult to assess whether the visibilities are consistent with 1.0 at zero baseline length. Meanwhile, the GRAVITY visibilities display a "hook" feature at the shortest effective baselines which we attribute to our deprojection. Observations probing shorter spatial frequencies are required to assess the flux contribution of any overresolved component to the visibilities. Here, we assume that this contribution is minimal and that the NIR emission probed by our interferometry arises purely from the sublimation rim at the inner edge of the disk.

We prescribe the density structure of the circumstellar material, $\rho(r, z)$, using the α-disk prescription of Shakura & Sunyaev (1973) whereby

$$\rho(r, z) = \frac{\Sigma(r)}{h(r)\sqrt{2\pi}} \exp\left\{-\frac{1}{2}\left[\frac{z}{h(r)}\right]^2\right\}. \quad (2)$$

Here, r and z are the radial distance into the disk and the vertical height above the disk midplane, respectively. The parameters $h(r)$ and $\Sigma(r)$ describe the scale height,

$$h(r) = h_0\left(\frac{r}{100\ \mathrm{au}}\right)^{\beta}, \quad (3)$$

and the surface density,

$$\Sigma(r) = \Sigma_0\left(\frac{r}{100\ \mathrm{au}}\right)^{-p}, \quad (4)$$

of the disk, respectively. Constants h_0 and Σ_0 are equated at $r = 100$ au. We keep $p = 1.0$ fixed in all models.

In adopting this approach, we do not account for any additional complexity in the radial dependence of the disk surface density and scale height, as evidenced by the apparent dust cavity at $\sim$18 au seen in CARMA images of RY Tau (Isella et al. 2010), for example. While we do not expect this to affect the modeling of the K-band visibilities, we discuss the implications of this approach in relation to the bulk SED in Section 4.1.

The final temperature structure of the disk and the shape of the dust sublimation front are then established in an iterative manner using the Lucy (1999) algorithm, provided T_{sub} is prescribed for each grain species in the model. We prescribe the disk models using a gas density-dependent sublimation temperature from Pollack et al. (1994):

$$T_{\mathrm{sub}} = G\rho^{\gamma}(r, z). \quad (5)$$

Here, $G = 2000$ K and $\gamma = 1.95 \times 10^{-2}$. This produces an inner rim that curves away from the star with increasing scale height above/below the disk midplane and whose innermost edge depends on the grains with the largest T_{sub} and cooling efficiency (Isella & Natta 2005). As T_{sub} and the cooling efficiency typically increase with increasing grain size, we populate the disk using dust of a single-grain size, which we denote a_{max}, which represents the largest grains which significantly contribute to the opacity in the disk rim. Importantly, this does not mean that grain growth beyond a_{max} has not occurred. Instead, any growth of grains beyond a_{max} simply does not contribute sufficiently to the opacity in the inner disk. We adopt a single-grain model (as in Isella & Natta 2005, for example) as opposed to a two-grain mixture model (as in Tannirkulam et al. 2007) to control the curvature of the inner rim. This provides a narrower inner disk rim (i.e., one that curves over a smaller range of disk annuli, Tannirkulam et al. 2007), but which speeds up model computation (Davies et al. 2018).

For consistency with Davies et al. (2018) and Labdon et al. (2019), only Draine (2003) silicates are used. Though this assumption is rather simplistic, it is reasonable considering the good fit provided to the Spitzer spectrum by models only considering silicate grains (Espaillat et al. 2011).

3.1.1. Stellar and Bulk Disk Parameters

The disk in our TORUS models is passively heated by a single star located at the grid center. Estimates of T_{eff}, the stellar radius, $R_{\star}$, stellar mass, $M_{\star}$, d, and A_V were required as model inputs. A range of values for RY Tau's stellar parameters have been published and cited throughout the literature, in part due to its photometric and spectroscopic temporal variability. The values adopted herein are presented in Table 3, and a brief discussion of the impact of using commonly adopted alternatives is presented in Section 4.3.

T_{eff} and $M_{\star}$ are taken from Calvet et al. (2004), while we revise their estimate of the stellar luminosity, $L_{\star}$, using the "bright" epoch photometry and A_V from Petrov et al. (2019). Through analyzing the V versus $(B - V)$ color–magnitude diagram produced using data obtained during their photometric monitoring campaign, Petrov et al. (2019) noted that the curved distribution of data points is similar in shape to those of objects exhibiting UX Ori-type behavior. However, the linear section of data points, which is typically observed for UX Ori-type objects when the central star is directly observable, is missing. They note that their A_V estimate—which is broadly consistent with previous estimates (e.g., Calvet et al. 2004; Herczeg & Hillenbrand 2014; Garufi et al. 2019)—likely provides an upper limit for A_V as a result. From T_{eff} and $L_{\star}$, we re-estimate $R_{\star}$ (3.2 $R_{\odot}$, see Table 3).

As a member of the Taurus star-forming region, RY Tau is typically considered to be located at $d \sim 140$ pc (Elias 1978). In apparent contrast, the estimate of d inferred from the Gaia DR2 parallax (Gaia Collaboration et al. 2016, 2018) suggests a much increased $d = 443^{+55}_{-44}$ pc (Bailer-Jones et al. 2018). However, the renormalized unit weight error, provided in Gaia DR2 as an assessment of the quality of the astrometric fit for each source (Galli et al. 2018), is 6.7. This indicates a less than ideal astrometric fit, likely related to the strong nebulosity present around RY Tau that impacts the Gaia point-spread function. For this reason, we adopt $d = 140$ pc in our modeling of RY Tau.

As our NIR observations (and the SED) are insensitive to the outer disk radius, R_{out}, we rely on the literature estimates of this quantity throughout our modeling, adopting $R_{\mathrm{out}} = 80$ au (Isella et al. 2010; Takami et al. 2013). Due to the simple grain prescription we adopt, we are also unable to meaningfully estimate the disk mass. Instead, we adopt a total disk mass of 0.3 $M_{\odot}$ (assuming a dust-to-gas ratio of 1:100) throughout, as this provided a reasonable fit to the submm portion of the SED.

3.1.2. Simulated Observations

Following convergence, model SEDs and K-band ($\lambda = 2.13\mu$m) images were computed using a separate Monte Carlo algorithm based on the optical properties of the specific dust species in each

Table 4
Prior Estimates of the Large-scale Disk Geometry

Reference	i_d (°)	PA_{major} (°)
Agra-Amboage et al. (2009)	45–76.5	24 ± 1
Isella et al. (2010)	66 ± 2	24 ± 3
Pinilla et al. (2018)	62	23
Long et al. (2018)	65.0 ± 0.02	23.06 ± 0.02
L19	65.0 ± 0.1	23.1 ± 0.1
G19	55	23

Note. Position angles are quoted for the disk major axis and are measured east of north. Parameters from Agra-Amboage et al. (2009) and G19 are determined from the microjet orientation, and assume the disk plane is perpendicular to this axis.

model (Harries et al. 2019). Model visibilities were extracted from the images at $PA_b = 0°$–180° and at baseline lengths up to 330 m, corresponding to the full range of spatial frequencies probed by our (u, v)-plane coverage. The model ϕ_{CP} were computed from the sum of visibility phases extracted from the image along each closed triangle of baseline vectors (see Davies et al. 2018 for more details).

Simulated images and SEDs were computed at $i_d = 65°$, based on the estimates of i_d from mm interferometry (see Table 4). Synthetic SEDs were computed at $i_d = 65°$ and a near face-on $i_d = 20°$, enabling us to asses the level of circumstellar extinction provided by each model. The simulated images were rotated so that $PA_{major} = 23°$ east of north, and the brighter side of the disk in each simulated image lay to the northwest to match the images obtained with HST (Agra-Amboage et al. 2009), VLT/SPHERE (G19), and Subaru/HiCIAO (Takami et al. 2013). PA_{minor} (113°) is also in good agreement with the microjet axis position angle observed by HST (St-Onge & Bastien 2008; Agra-Amboage et al. 2009) and VLT/SPHERE (G19), indicating no strong evidence for misalignment between the inner and outer disk regions.

3.2. The Nature of the Circumstellar K-band Emission

The stellar (Table 3) and bulk disk parameters ($R_{out} = 80$ au; $M_{disk} = 0.30\,M_\odot$; see Section 3.1.1) were kept fixed throughout our TORUS modeling. We investigated different values of the maximum grain size contributing to the opacity in the inner disk, a_{max}, together with the scale height constant, h_0, and flaring parameter, β. Together, these variables control the location, size, and shape of the NIR-emitting inner disk.

We performed an initial exploration of a broad range of model parameters to explore their interdependence. We assessed the goodness-of-fit of each model using the following procedure:[13]

1. the model visibilities were inspected by-eye to check for consistency with the overall shape of the observed visibilities and the minimum observed visibility level;
2. the model SED across optical and NIR wavelengths was compared with the data to ensure it fell within the range between the "bright" and "faint" epoch optical and NIR photometry; and
3. if the model passed these checks, the goodness-of-fit of the model to the visibilities was evaluated using the χ^2_r statistic.

These assessments were then used to select the values to be explored on the next iteration of models. This resulted in a sparsely sampled set of models with a_{max} ranging between 0.10 and 1.20 μm, h_0 ranging between 4 and 14 au, and β ranging between 0.88 and 1.40. In total, we explored ∼150 different combinations of values for these parameters.

Based on the results from this initial suite of models, we refined our model exploration around promising regions of the a_{max}–h_0–β parameter space, and computed a finer grid of TORUS models with $5 \leqslant h_0 \leqslant 9$ au, $0.88 \leqslant \beta \leqslant 1.03$, and $0.16 \leqslant a_{max} \leqslant 0.60$ μm. Above $h_0 \approx 9$ au, we found models were unable to simultaneously fit the visibilities and the optical-to-NIR region of the SED. Instead, the NIR flux in the SED was consistently underestimated by the models, even when the model visibilities provided a reasonable fit to those observed. Meanwhile, a surprising behavior of models with low a_{max} set the lower limit to the range of h_0 values we explored: for models with $a_{max} \lesssim 0.16$ μm, we found the inner edge of the disk rim moves *inward* with decreasing a_{max} (see Appendix B), opposite to what happens for larger grains ($a_{max} \gtrsim 0.16$ μm). This effect has not been reported by studies conducting similar analyses for hotter stars (e.g., Isella & Natta 2005; Davies et al. 2018). Further investigation of this effect is outside the scope of this paper, and is deferred to future study (C. L. Davies & T. J. Harries 2020, in preparation).

Our analysis shows that the circumstellar K-band-emitting region is consistent with models of a disk inner edge shaped by dust sublimation. Our best-fit model suggests that the dust rim extends inward to within 0.206 ± 0.001 au of the central star, corresponding to R_{sub} for silicate dust with $a_{max} = 0.40$ μm. Specifically, the model providing the best fit to the visibility data has $a_{max} = 0.40$ μm, $h_0 = 8$ au, and $\beta = 0.99$. The quoted uncertainty of ±0.001 au is equivalent to half a grid cell on our adaptive mesh (see Section 4.2 for a more detailed discussion of the uncertainty on our assessment of R_{sub}).

We display the corresponding TORUS model image (top left panel), SED (top middle panel), ϕ_{CP} (top right panel), and visibilities (lower panels) in Figure 4. The visibilities are split by PA_b to show the relative goodness-of-fit across different segments of the disk. The full SED (from optical to millimeter wavelengths) is shown to illustrate the goodness-of-fit of our model across the optical and NIR, while also demonstrating how our adoption of radial power laws for the scale height and surface density (Equations (3)) and (4), respectively) underestimates the flux at longer wavelengths. We discuss the implications of this in more detail below.

4. Discussion

4.1. RY Tau as a Pretransitional Disk

Figure 4 clearly shows that our best-fit model provides a poor fit to the SED at wavelengths longer than ∼10 μm. This behavior is seen across all of the models we explored, and is not unexpected: the shape of the SED of RY Tau has led previous studies to classify the circumstellar structure as a pretransitional disk (Furlan et al. 2009; Espaillat et al. 2011). Moreover, CARMA and ALMA images of RY Tau have highlighted the likely presence of a dust cavity or gap within ∼18 au (Isella et al. 2010; Long et al. 2018; L19). The disk

[13] We note that the SED beyond NIR wavelengths was largely ignored in this procedure, as we do not expect Equations (3) and (4) to fully prescribe the radial dependence of the scale height and the surface density, respectively.

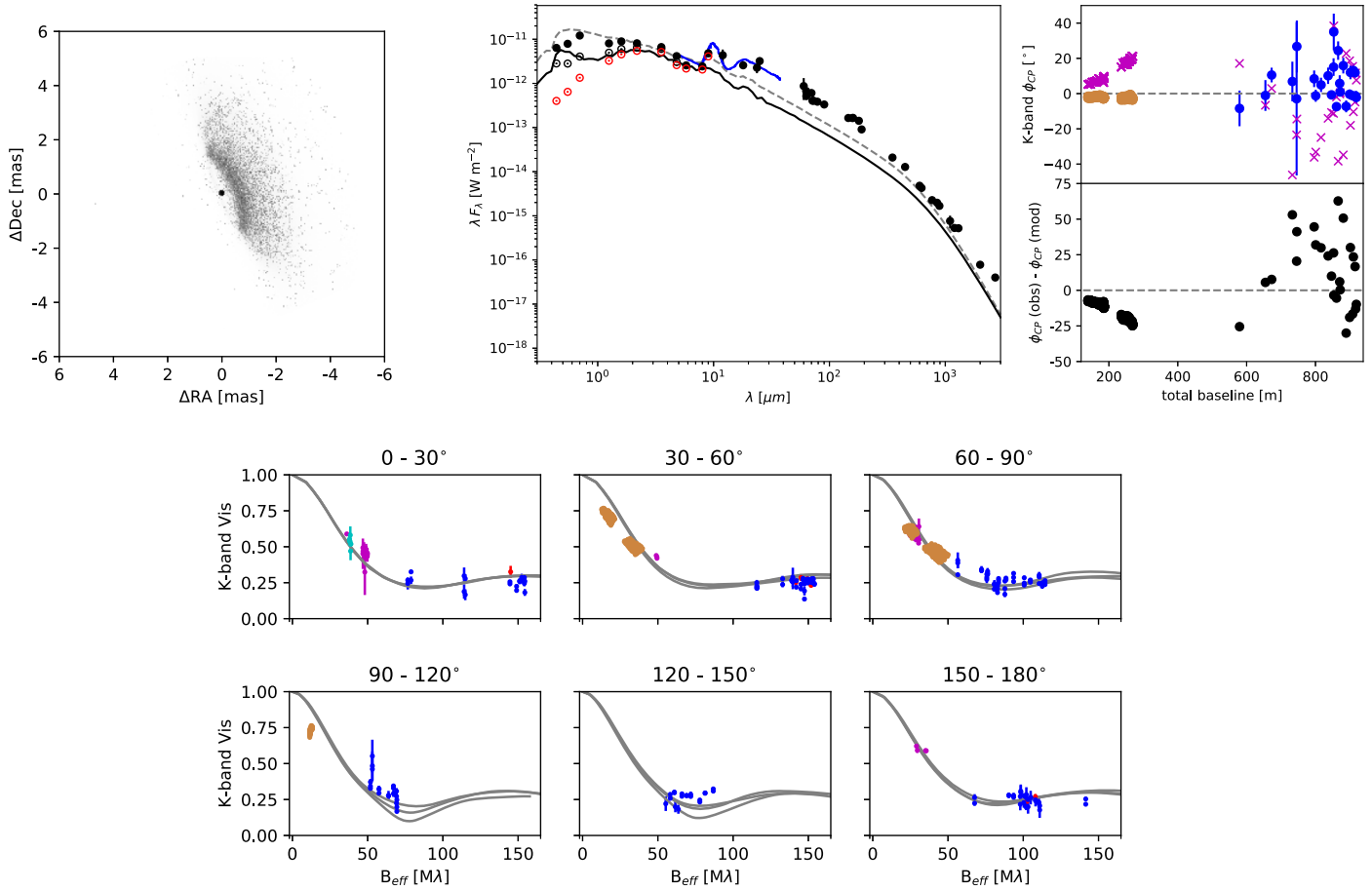

Figure 4. TORUS model providing the best fit to the visibilities ($h_0 = 8$ au; $\beta = 0.99$ and $a_{\max} = 0.40$ μm). The TORUS model 2.13 μm image (top left) was computed at $i_d = 65°$ and rotated such that $PA_{major} = 23°$. The SED (top middle) compares the data from Figure 2 with the TORUS model computed at $i_d = 65°$ (solid black line) and a more face-on $i_d = 20°$ (dashed gray line) to highlight the amount of local extinction provided by the disk rim. The ϕ_{CP} (upper panel) and their residuals (lower panel) are displayed in the top right. Orange and blue data points have the same meaning as in Figure 1, while pink crosses indicate the model values extracted from the image. The lower two panels show the visibilities (colors as in Figure 1) compared with the visibility curves extracted from the model image at increments of 10° in PA_b (solid gray lines). Visibilities are split according to PA_b (the range is labeled above each subplot).

structure is thus expected to deviate from the radial power laws we have used for the scale height and the surface density in our TORUS models (Equations (3) and (4), respectively). In addition, extrapolating the single-grain size dust model of the inner dust rim to the full disk impacts on the outer disk emissivity, as well as the strength and shape of the silicate feature.

4.2. *Uncertainty Estimate for* R_{sub}

We display the comparative goodness-of-fit of our grid of models to the observed visibilities as χ^2_r maps in Figure 5. Hatched grid cells highlight areas of the map that provided poorer fits to the data than the maximum χ^2_r value indicated by the color bar. White cells highlight unexplored regions of our model parameter space. As the number of data points provided by the GRAVITY observations far exceeds the number provided by CLASSIC and CLIMB, the short-baseline data dominate the assessment of the goodness-of-fit. To combat this, we also calculated the goodness-of-fit to the CHARA visibilities only (Figure 6).

Some models that used different combinations of h_0, β and/or $a_{\max}$ produced similarly good fits to the visibilities. In these models, the steeper increase in scale height with respect to disk radius, provided by decreasing β, was counteracted by the reduction in h_0 (or vice versa). For example, the model with $h_0 = 8$ au, $\beta = 0.99$, and $a_{\max} = 0.36$ μm (see Figure 7) produces only a marginally poorer fit to the short-baseline visibilities ($\chi^2_r = 1.843$ compared with $\chi^2_r = 1.841$), while the goodness-of-fit provided to the CHARA visibilities is poorer than in our best-fit model ($\chi^2_r = 2.633$ compared with $\chi^2_r = 1.606$).

The short-baseline data are the most sensitive to $a_{\max}$ as they trace the fall-off in visibility with increasing spatial frequency. From Figure 5, we see that our assessment of $a_{\max}$ is reasonably robust. With the exception of the $h_0 = 5$ au models, which all provide similarly poor fits to the visibilities, the best-fitting model in each χ^2_r map has $a_{\max} = 0.36 - 0.40$ μm. Based on the results from all of our models, we estimate $R_{sub} = 0.210 \pm 0.005$ au. Larger grains produce inner disk rims that are underresolved compared with our data, while smaller grains produce comparatively overresolved rims. However, it is important to note that this result does not rule out grain growth to larger sizes. Instead, our result indicates that the number density of silicate grains larger than 0.40 μm in the inner disk rim is insufficient for these grains to contribute significantly to the opacity at the inner disk. Furthermore, due to their associated optical properties, our observations are

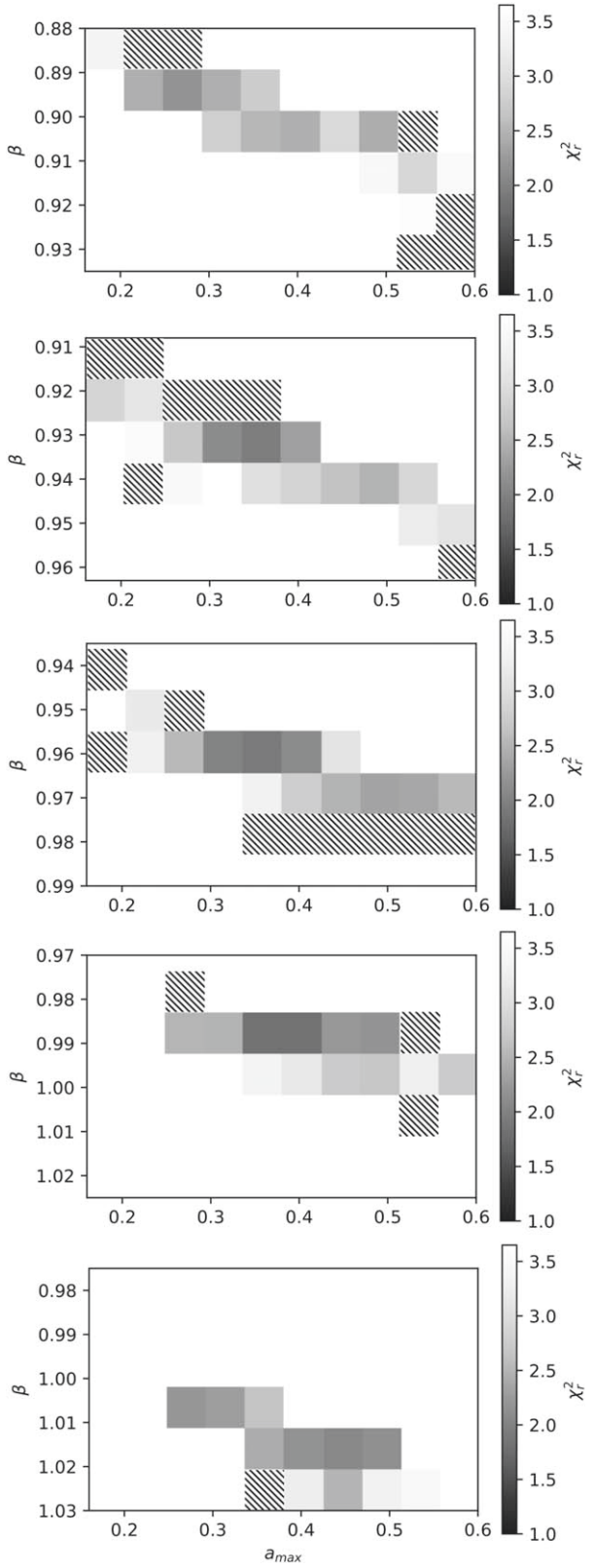

Figure 5. χ^2_r maps for models with different maximum grain sizes (a_{max}; x-axis) and scale height constants (from top to bottom: $h_0 = 5$, 6, 7, 8, and 9 au) and flaring parameters (β; y-axis) when considering fits to all the data (i.e., 798 degrees of freedom) and a 10% systematic error on the visibility measurements. Models that provided poor fits to the data (i.e., χ^2_r exceeded the range plotted) are shown as hatched boxes.

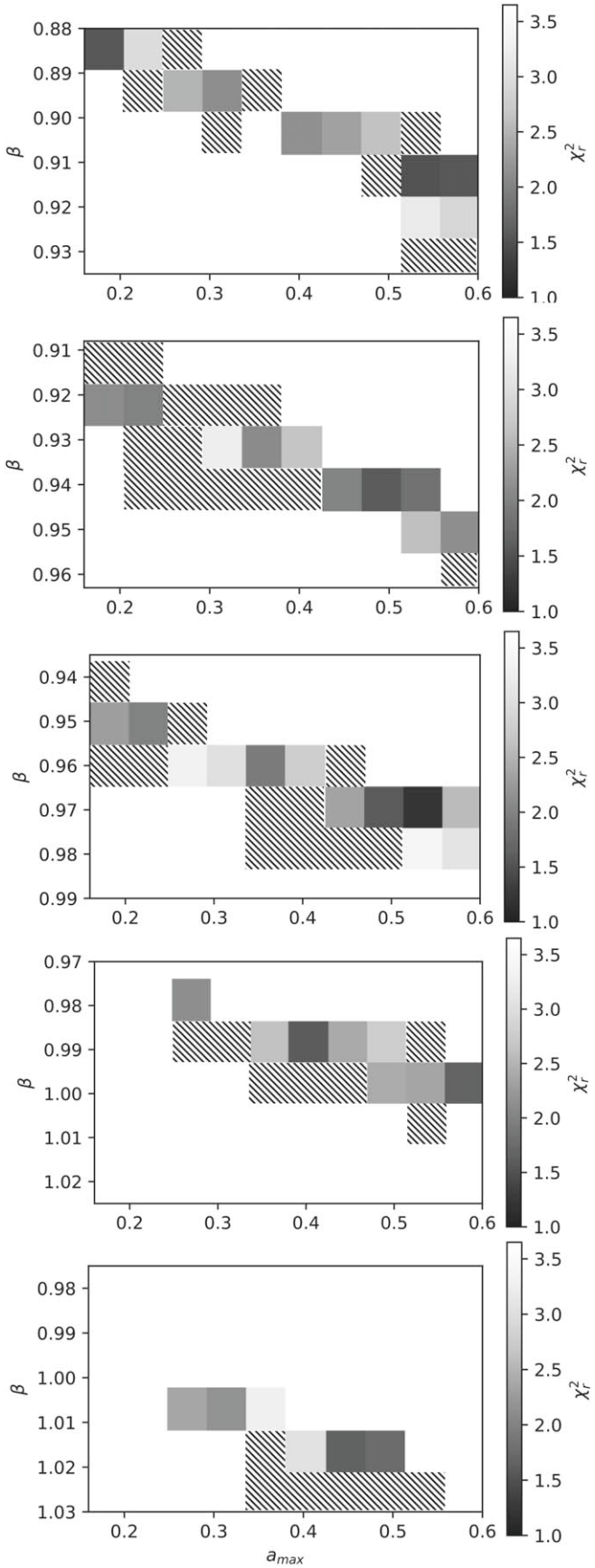

Figure 6. As in Figure 5, but considering only the CHARA (CLASSIC and CLIMB) data in the fitting process (i.e., 171 degrees of freedom). The additional 10% systematic error to the visibilities is still included.

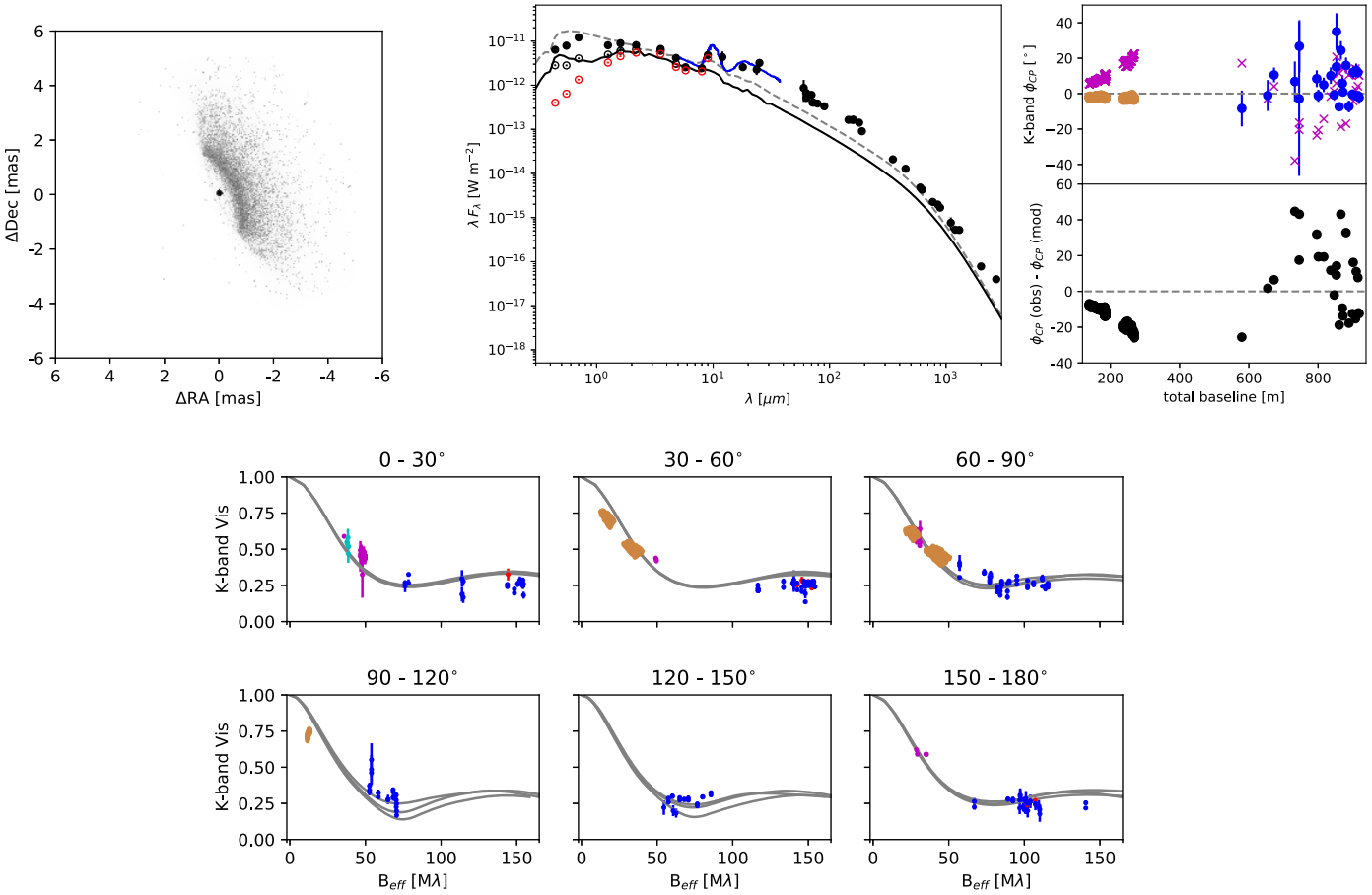

Figure 7. As in Figure 4, but for the TORUS model with $h_0 = 8$ au; $\beta = 0.99$ and $a_{\max} = 0.36$ μm).

insensitive to the presence of grains larger than $\sim$1.2 μm (see Isella & Natta 2005).

4.3. Sensitivity of Our Results to the Adopted Stellar Input Parameters

Our modeling in previous sections relies to a certain extent on the assumption that the stellar parameters we have adopted are representative of the true values. As we outlined in Section 3.1.1, accurately assessing values for $T_{\rm eff}$, $L_\star$, d, and A_V for RY Tau is complicated by photometric variability and direct occultation by the disk surface layers. In this subsection, we briefly assess the sensitivity of our results to the stellar parameters adopted.

In Table 3, we provide example alternative stellar parameters for RY Tau, recently adopted in L19 and G19. L19 co-added 96 archival ESPaDOnS spectra and compared them with F and G spectral type BT-Settl models with solar metallicity and surface gravity, $\log g = 4.0$. They yielded $T_{\rm eff} = 6220 \pm 80$ K (comparable with F6–F8 spectral types using Kenyon & Hartmann (1995) spectral type-to-$T_{\rm eff}$ relations). This is a small change in spectral type from the more commonly adopted values of G0 (Herczeg & Hillenbrand 2014) and G1 (Calvet et al. 2004). G19 also re-estimated $T_{\rm eff}$, comparing four archival high-resolution William Herschel Telescope UES spectra to synthetic atmosphere models computed from the ATLAS and SYNTHE codes and finding $T_{\rm eff} = 5750$ K with $\log g = 3.58$, closer to our adopted values ($T_{\rm eff} = 5945$ K with $\log g = 3.8$).

L19 estimated $A_V = 1.94 \pm 0.2$ mag, higher than our adopted value of 1.6 mag while G19 estimated $A_V = 1.5$ mag. For d, L19 and G19 both assessed the Gaia parallaxes of the 29 closest Taurus members to RY Tau, computing an average Gaia distance of 128.5 ± 0.3 pc. L19 adopted this value for RY Tau while G19 used this calculation to argue the case for adopting the Hipparcos value ($d = 133$ pc). Based on these differences, the estimates of $L_\star$ from these two studies then differ greatly with L19 estimating $L_\star = 12.3\,L_\odot$ and G19 estimating $L_\star = 6.3\,L_\odot$.

Combined with our best-fitting disk model from Section 3.2, the different stellar input parameters produce model SEDs with similar shapes but different intensities. The model using G19 stellar parameters has an $R_{\rm sub}$ consistent with our estimate above (0.212 au). Meanwhile, the flux across the IR provided by the L19 model underestimates that in the SED compiled from archival photometry. If these stellar parameters are closer to RY Tau 's true values, this indicates that less of the line-of-sight extinction is provided by circumstellar material than in our best-fit disk model. Using our best-fit disk model with L19 stellar parameters produces a less-extended inner rim, with $R_{\rm sub} \approx 0.166$ au. The poor fit to the visibilities provided by this model indicates that this is not a good estimate. Decreasing $a_{\max}$ to 0.20 μm provides an improved fit with $R_{\rm sub} \approx 0.210$ once again. Thus, it appears our estimate of $R_{\rm sub}$ is reasonably robust against differences in stellar parameter estimates.

4.4. Comparison of R_{sub} with the Theoretical Magnetospheric Truncation Radius

To further characterize the inner disk of RY Tau, we calculate and compare the magnetospheric truncation radius,

$R_{\rm trunc}$, with the value of $R_{\rm sub}$ inferred from our TORUS modeling. The magnetospheric truncation radii of Herbig Ae stars are typically far interior to $R_{\rm sub}$, leaving a portion of the inner disk completely devoid of Silicate grains.[14] However, for lower mass, T-Tauri stars, the locations of $R_{\rm trunc}$ and $R_{\rm sub}$ may overlap, leading to the possibility of dust being lifted into magnetospheric accretion streams (e.g., Bodman et al. 2017) and producing a warped inner disk where the scale height, measured with respect to a reference disk midplane, varies with azimuth (e.g., Kesseli et al. 2016). In light of this, we calculate $R_{\rm trunc}$ and compare it with our estimate of $R_{\rm sub}$ to assess the applicability of the azimuthally invariant scale height prescription (Equation (3)).

Considering the force balance between the outward pressure from the large-scale stellar magnetic field, $B_\star$, and the inward pressure from mass accretion through the disk (e.g., Johnstone et al. 2014),

$$R_{\rm trunc} = c(2GM_\star)^{-1/7}\dot{M}_{\rm acc}^{-2/7}\mu_1^{4/7}. \quad (6)$$

Here, G is the gravitational constant, $\dot{M}_{\rm acc}$ is the mass accretion rate through the disk, and μ_1 is the dipole moment.[15] The constant, c, accounts for the difference between spherical infall and magnetospheric accretion along columns. If $B_\star$ is dominated by dipolar fields (a good approximation at sufficient distances from the star due to the increased fall-off with radius of higher order fields) and the disk axis is perpendicular to the stellar magnetic field axis, $c = 0.5$ (Long et al. 2005) and $\mu_1 = B_{\rm dip}R_\star^3$ at equatorial regions. Here, $B_{\rm dip}$ is the strength of the dipole component of $B_\star$ at the stellar equator and $R_\star$ the stellar radius, as before. We note that in reality, higher order fields become important for small $R_{\rm trunc}$ (i.e., high mass accretion rates or low magnetic field strengths, for a given $M_\star$; Gregory et al. 2016), but we only consider the case of a dipole field here for simplicity.

RY Tau was observed using Zeeman–Doppler imaging as part of the Magnetic Protostars and Planets project (PI: J.-F. Donati) with a dipole magnetic field strength, $B_{\rm dip} \sim 300$ G measured in preliminary analysis (J.-F. Donati 2020, private communication). Assuming the stellar mass accretion rate ($6.4–9.1 \times 10^{-8}\,M_\odot$ yr^{-1}; Calvet et al. 2004) is a good first approximation for $\dot{M}_{\rm acc}$, we estimate $R_{\rm trunc} \approx 0.009–0.014$ au. This is an order of magnitude closer to the star than our estimate of $R_{\rm sub}$ (0.210 ± 0.005 au), indicating we are fine to assume an azimuthally symmetric scale height prescription to the inner disk edge.

5. Conclusions

We find that the K-band visibilities and optical-to-NIR SED of RY Tau are consistent with Monte Carlo radiative transfer models comprising a central star illuminating a passive disk with an inner edge shaped by dust sublimation with $R_{\rm sub} = 0.210 \pm 0.005$ au. The location of the inner rim is consistent with the sublimation radius of a disk where the largest grains contributing to the opacity (and thus controlling the rim location) are 0.36–0.40 μm. The growth of dust grains beyond 0.40 μm cannot be ruled out, but our results show that such grains do not contribute significantly to the opacity in the inner rim of the disk.

Interestingly, Labdon et al. (2019) found that the location of the inner disk of SU Aur is similarly controlled by the sublimation of 0.40 μm grains while Davies et al. (2018) found that larger (1.2 μm) grains were required to reproduce their H- and K-band interferometric observations of HD 142666. Both SU Aur and HD 142666 are similar in mass ($\sim 2\,M_\odot$) to RY Tau, while HD 142666 is older (>10 Myr; Dionatos et al. 2019) and more luminous ($\sim 20\,L_\odot$; Davies et al. 2018) than SU Aur and RY Tau (both ~ 2 Myr as members of the Taurus-Auriga star-forming region (Luhman 2018) and $\sim 12\,L_\odot$). Similar analyses of a greater number of disk-hosting YSOs are required before we can comment on whether this is possibly symptomatic of, for example, an evolutionary sequence for disks or that dust grains have to be larger to have survived as long as they have done around HD 142666.

While our models provide a good fit to the optical-to-NIR portion of the SED of RY Tau, they consistently poorly fit the data at longer wavelengths ($\gtrsim 10$ μm). This is due to the combined effect of populating our disk models with dust of a single-grain size and assuming the disk temperature and density can be prescribed using simple radial power laws (Section 3.1). Previous analysis of the SED (e.g., Furlan et al. 2009; Espaillat et al. 2011) and mm interferometry (Isella et al. 2010) of RY Tau has revealed the presence of at least one annular cavity at a separation of ~ 18 au from the central star. Thus, there is likely a deviation from simple radial power laws in temperature and density at a certain disk radius. MIR interferometric observations of RY Tau with the VLTI's MATISSE instrument (Lopez et al. 2014), for example, are required to further assess the structure of the disk between the sublimation rim and the outer disk regions probed by CARMA and ALMA.

We used existing measurements of the mass accretion rate and large-scale dipolar magnetic field strength of RY Tau to estimate a disk truncation radius of 0.009–0.014 au. This indicates that, while the dusty portion of the disk has an inner boundary at 0.210 ± 0.005 au due to sublimation, the gaseous portion of the disk may theoretically extend an order of magnitude closer to the star. Furthermore, this also validates our assumption of an azimuthally symmetric dust rim as it shows that dust is unlikely to survive close enough to the star to be lofted into magnetospheric accretion streams.

Our CHARA data was obtained over a 4-yr period, but our analysis reveals no direct evidence of temporal variability in the disk of RY Tau. Instead, the vertical spread in visibility across baselines probed by our CHARA observations is more likely attributed to measurement and calibration uncertainties. However, our exploration of the $a_{\rm max}$–h_0–β model parameter space in Section 3.2 highlights that models that produce a disk that is too shallow or too extended to directly occult the central star can be ruled out. These models consistently overestimate the visibilities on the baselines probed by our CHARA observations, indicating the stellar contribution to the flux contrast in the underlying brightness distribution is too high. In their analysis of RY Tau 's photometric variability, Petrov et al. (2019) drew similar conclusions and suggested the observer's line of sight to the stellar photosphere was partially occulted even during RY Tau 's brightest epochs. Furthermore, our results support previous claims based on (i) the timescales of quasi-periodic optical

[14] We explicitly mention silicate grains here, as if more refractory grains are present, they will be able to survive closer to the star at higher temperatures.
[15] This equation implicitly assumes the adoption of cgs units.

brightness variations (Zajtseva 2010); (ii) the correlation between outflow velocity and circumstellar accretion (Babina et al. 2016); and (iii) the seesaw-like variability in the Spitzer spectrum (Espaillat et al. 2011) that it is the surface layers of the inner disk, close to the dust sublimation rim, that provides this occulting surface.

While we are unable to comment on the possible intrinsic variability of the central star, the direct line-of-sight occultation of the star by the disk provides a mechanism by which structural changes in the surface layers of the dusty portion of the disk can give rise to the aperiodic brightness fluctuations observed across optical and IR wavelengths. The increased sensitivity of the six-telescope MIRC-X combiner (Anugu et al. 2018; Kraus et al. 2018) at the CHARA Array provides an exciting opportunity to search for such structural changes in the disk of this object and others showing aperiodic photometric variability.

We thank the anonymous referee whose comments ensured greater clarity in the presentation of our results. C.L.D. and S.K. acknowledge support from the ERC Starting Grant "ImagePlanetFormDiscs" (grant Agreement No. 639889). R.G.L. acknowledges support by Science Foundation Ireland under grant No. 18/SIRG/5597. We thank Bernard Lazareff, Jean-Baptiste Le Bouquin and Rachel Akeson for their assistance in acquiring archival data and University of Exeter summer research project student Daniel J. Barker for his assistance in incorporating automatic VisIt plotting functionality into the analysis pipeline. C.L.D. thanks Aaron Labdon, Scott Gregory, Jean-Francois Donati, Francois Menard and Catherine Dougados for helpful discussions. This work is based upon observations obtained with the Georgia State University Center for High Angular Resolution Astronomy (CHARA) Array at Mount Wilson Observatory and data obtained from the ESO Science Archive Facility. The CHARA Array is supported by the National Science Foundation under grant No. AST-1636624 and AST-1715788. Institutional support has been provided from the GSU College of Arts and Sciences and the GSU Office of the Vice President for Research and Economic Development. The calculations for this paper were performed on the University of Exeter Supercomputer, a DiRAC Facility jointly funded by STFC, the Large Facilities Capital Fund of BIS, and the University of Exeter. This research has made use of: the NASA/IPAC Infrared Science Archive, which is operated by the Jet Propulsion Laboratory, California Institute of Technology, under contract with the National Aeronautics and Space Administration (NASA); the Keck Observatory Archive (KOA), which is operated by the W. M. Keck Observatory and the NASA Exoplanet Science Institute (NExScI), under contract with NASA; the Jean-Marie Mariotti Center `OiDB` service;[16] the SIMBAD database, operated at CDS, Strasbourg, France; the VizieR catalog access tool, CDS, Strasbourg, France; NASA's Astrophysics Data System Bibliographic Services. This work has made use of services produced by the NASA Exoplanet Science Institute at the California Institute of Technology. The Palomar Testbed Interferometer was operated by the NASA Exoplanet Science Institute and the PTI collaboration. It was developed by the Jet Propulsion Laboratory, California Institute of Technology with funding provided from NASA.

Facilities: VLTI, CHARA, Keck, PTI.

Software: TORUS (Harries et al. 2019), pysynphot (STScI Development Team 2013), NumPy (VanDerWalt et al. 2011), matplotlib (Hunter 2007), Astropy (Astropy Collaboration et al. 2013).

[16] Available at http://oidb.jmmc.fr.

Appendix A
Multiband Photometry Used to Build the SED

The multiband photometry used to build the SED of RY Tau, together with their individual references, are shown in Tables A1 and A2.

Table A1
Adopted "Bright" and "Faint" Optical and IR Photometric Magnitudes, Taken from Petrov et al. (2019)

Date	*B*	*V*	*R*	*J*	*H*	*K*	*L*	*M*
1989 Oct 25	11.20	10.09	8.96	7.15	6.12	5.26	4.09	3.70
2016 Nov 11	12.08	11.21	10.15	7.68	6.55	5.50	4.19	4.03

Table A2
Additional Photometry Retrieved from the Literature with Measurement Uncertainties where Reported

λ (μm)	Flux (Jy)	References
5.8	4.2	Cieza et al. (2009)
8.0	5.50	Cieza et al. (2009)
9.0	12.28 ± 0.07	Abrahamyan et al. (2015)
12.0	12.73	Moshir et al. (1990)
18.0	15.43 ± 0.14	Abrahamyan et al. (2015)
23.68	17.86 ± 4.42	Robitaille et al. (2007)
25.0	26.70 ± 5.00	Moshir et al. (1990)
60.0	17.40 ± 9.00	Moshir et al. (1990)
63.0	14.10 ± 0.05	Keane et al. (2014)
63.18	10.86 ± 0.07	Howard et al. (2013)
70.0	14.13 ± 1.40	Howard et al. (2013)
71.42	9.63 ± 0.96	Robitaille et al. (2007)
72.84	9.82 ± 0.03	Howard et al. (2013)
78.74	10.10 ± 0.04	Howard et al. (2013)
90.16	10.00 ± 0.04	Howard et al. (2013)
100.0	36.50 ± 25.00	Moshir et al. (1990)
145.53	7.98 ± 0.02	Howard et al. (2013)
157.74	8.64 ± 0.03	Howard et al. (2013)
160.0	8.81 ± 0.88	Howard et al. (2013)
179.53	8.50 ± 0.04	Howard et al. (2013)
189.57	5.73 ± 0.11	Howard et al. (2013)
350.0	2.44 ± 0.33	Andrews & Williams (2005)
450.0	1.92 ± 0.16	van der Marel et al. (2016)
600.0	0.96 ± 0.04	Mannings & Emerson (1994)
624.0	0.89 ± 0.14	Beckwith & Sargent (1991)
769.0	0.58 ± 0.04	Beckwith & Sargent (1991)
850.0	0.56 ± 0.03	van der Marel et al. (2016)
890.0	0.50 ± 0.03	Andrews et al. (2013)
1100.0	0.28 ± 0.09	Mannings & Emerson (1994)
1200.0	0.21 ± 0.02	Altenhoff et al. (1994)
1300.0	0.227 ± 0.007	Isella et al. (2010)
2000.0	0.052 ± 0.006	Kitamura et al. (2002)
2700.0	0.036 ± 0.003	Isella et al. (2010)

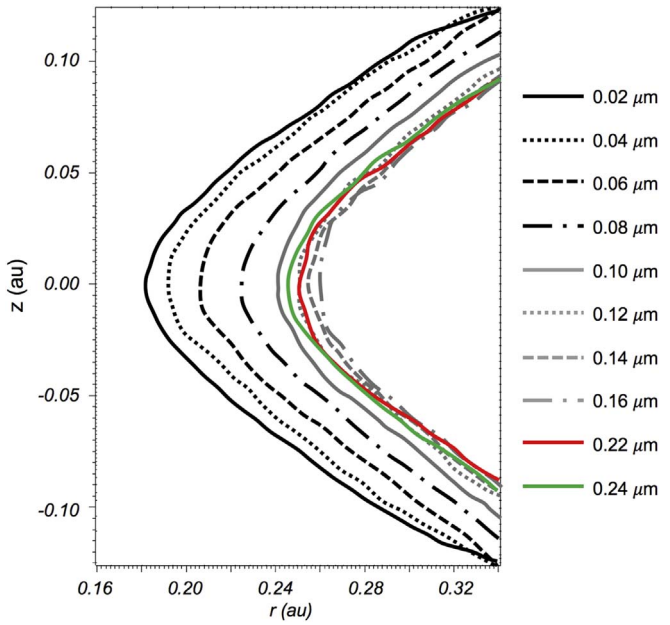

Figure A1. Inner rim shape and location for models computed with $a_{\max}$ between 0.02 and 0.16 μm (various black and gray lines; see the key on the right for details) compared with models with $a_{\max} = 0.22$ μm (red line) and $a_{\max} = 0.24$ μm (green line). All models were run with $h_0 = 9$ au and $\beta = 1.02$, the same as in our best-fit model (see Section 3.2).

Appendix B
Sublimation Rim Location Dependence on Grain Size

We uncovered surprising behavior of the dependence of the location of $R_{\rm sub}$ and the grain size when $a_{\max} < 0.16$ μm. In Figure A1, we show the location and shape of the inner edge of the rim for $a_{\max}$ between 0.02 and 0.16 μm and compare these with models with $a_{\max} = 0.22$ μm and $a_{\max} = 0.24$ μm which behave as expected. Rim shapes for models with $a_{\max} = 0.18$ μm and $a_{\max} = 0.20$ μm were indistinguishable from the model with $a_{\max} = 0.16$ μm and are thus not shown in the plot. Between 0.02 μm and $\approx$0.16 μm, the inner rim location moves further from the star with increasing $a_{\max}$, opposite to what is expected and which has been reported for similar studies of hotter stars (Isella & Natta 2005; Davies et al. 2018). Models including grains larger than $\approx$0.16 μm maintain the behavior which we expect to see: the inner rim location moves closer to the star with increasing $a_{\max}$. Further investigation into the reasons for this are outside the scope of this paper and are deferred to future study (Davies & Harries 2020, in preparation).

ORCID iDs

Claire L. Davies https://orcid.org/0000-0001-9764-2357
Stefan Kraus https://orcid.org/0000-0001-6017-8773
Tim J. Harries https://orcid.org/0000-0001-8228-9503
John D. Monnier https://orcid.org/0000-0002-3380-3307
Brian Kloppenborg https://orcid.org/0000-0003-0350-5453
Alicia Aarnio https://orcid.org/0000-0002-1327-9659
Rebeca Garcia Lopez https://orcid.org/0000-0002-2144-0991
Rafael Millan-Gabet https://orcid.org/0000-0003-0447-5866
Theo A. ten Brummelaar https://orcid.org/0000-0002-0114-7915
Yamina Touhami https://orcid.org/0000-0002-8627-2415

References

Abrahamyan, H. V., Mickaelian, A. M., & Knyazyan, A. V. 2015, A&C, 10, 99
Agra-Amboage, V., Dougados, C., Cabrit, S., Garcia, P. J. V., & Ferruit, P. 2009, A&A, 493, 1029
Akeson, R. L., Ciardi, D. R., van Belle, G. T., Creech-Eakman, M. J., & Lada, E. A. 2000, ApJ, 543, 313
Akeson, R. L., Walker, C. H., Wood, K., et al. 2005, ApJ, 622, 440
Altenhoff, W. J., Thum, C., & Wendker, H. J. 1994, A&A, 281, 161
Andrews, S. M., Rosenfeld, K. A., Kraus, A. L., & Wilner, D. J. 2013, ApJ, 771, 129
Andrews, S. M., & Williams, J. P. 2005, ApJ, 631, 1134
Anugu, N., Le Bouquin, J.-B., Monnier, J. D., et al. 2018, Proc. SPIE, 10701, 1070124
Astropy Collaboration, Robitaille, T. P., Tollerud, E. J., et al. 2013, A&A, 558, A33
Babina, E. V., Artemenko, S. A., & Petrov, P. P. 2016, AstL, 42, 193
Bailer-Jones, C. A. L., Rybizki, J., Fouesneau, M., Mantelet, G., & Andrae, R. 2018, AJ, 156, 58
Beckwith, S. V. W., & Sargent, A. I. 1991, ApJ, 381, 250
Bodman, E. H. L., Quillen, A. C., Ansdell, M., et al. 2017, MNRAS, 470, 202
Bonneau, D., Clausse, J.-M., Delfosse, X., et al. 2006, A&A, 456, 789
Bonneau, D., Delfosse, X., Mourard, D., et al. 2011, A&A, 535, A53
Calvet, N., Muzerolle, J., Briceño, C., et al. 2004, AJ, 128, 1294
Cieza, L. A., Padgett, D. L., Allen, L. E., et al. 2009, ApJL, 696, L84
Colavita, M. M., Wallace, J. K., Hines, B. E., et al. 1999, ApJ, 510, 505
Colavita, M. M., Wizinowich, P. L., Akeson, R. L., et al. 2013, PASP, 125, 1226
Davies, C. L., Kraus, S., Harries, T. J., et al. 2018, ApJ, 866, 23
Dionatos, O., Woitke, P., Güdel, M., et al. 2019, A&A, 625, A66
Draine, B. T. 2003, ApJ, 598, 1026
Duvert, G., Young, J., & Hummel, C. A. 2017, A&A, 597, A8
Elias, J. H. 1978, ApJ, 224, 857
Espaillat, C., Furlan, E., D'Alessio, P., et al. 2011, ApJ, 728, 49
Furlan, E., Watson, D. M., McClure, M. K., et al. 2009, ApJ, 703, 1964
Gaia Collaboration, Brown, A. G. A., Vallenari, A., et al. 2018, A&A, 616, A1
Gaia Collaboration, Prusti, T., de Bruijne, J. H. J., et al. 2016, A&A, 595, A1
Galli, P. A. B., Loinard, L., Ortiz-Léon, G. N., et al. 2018, ApJ, 859, 33
Garufi, A., Podio, L., Bacciotti, F., et al. 2019, A&A, 628, A68
Grankin, K. N., Melnikov, S. Y., Bouvier, J., Herbst, W., & Shevchenko, V. S. 2007, A&A, 461, 183
Gravity Collaboration, Abuter, R., Accardo, M., et al. 2017, A&A, 602, A94
Gravity Collaboration, Perraut, K., Labadie, L., et al. 2019, A&A, 632, A53
Gregory, S. G., Donati, J.-F., & Hussain, G. A. J. 2016, arXiv:1609.00273
Harries, T. J. 2000, MNRAS, 315, 722
Harries, T. J., Haworth, T. J., Acreman, D., Ali, A., & Douglas, T. 2019, A&C, 27, 63
Haubois, X., Bernaud, P., Mella, G., et al. 2014, Proc. SPIE, 9146, 91460O
Herczeg, G. J., & Hillenbrand, L. A. 2014, ApJ, 786, 97
Houck, J. R., Roellig, T. L., van Cleve, J., et al. 2004, ApJS, 154, 18
Howard, C. D., Sandell, G., Vacca, W. D., et al. 2013, ApJ, 776, 21
Hunter, J. D. 2007, CSE, 9, 90
Isella, A., Carpenter, J. M., & Sargent, A. I. 2010, ApJ, 714, 1746
Isella, A., & Natta, A. 2005, A&A, 438, 899
Johnstone, C. P., Jardine, M., Gregory, S. G., Donati, J.-F., & Hussain, G. 2014, MNRAS, 437, 3202
Kama, M., Min, M., & Dominik, C. 2009, A&A, 506, 1199
Keane, J. T., Pascucci, I., Espaillat, C., et al. 2014, ApJ, 787, 153
Kenyon, S. J., Dobrzycka, D., & Hartmann, L. 1994, AJ, 108, 1872
Kenyon, S. J., & Hartmann, L. 1995, ApJS, 101, 117
Kesseli, A. Y., Petkova, M. A., Wood, K., et al. 2016, ApJ, 828, 42
Kitamura, Y., Momose, M., Yokogawa, S., et al. 2002, ApJ, 581, 357
Kraus, S., Monnier, J. D., Anugu, N., et al. 2018, Proc. SPIE, 10701, 1070123
Kurucz, R. L. 1979, ApJS, 40, 1
Labdon, A., Kraus, S., Davies, C. L., et al. 2019, A&A, 627, A36
Lazareff, B., Berger, J.-P., Kluska, J., et al. 2017, A&A, 599, A85
Lebouteiller, V., Barry, D. J., Spoon, H. W. W., et al. 2011, ApJS, 196, 8
Long, F., Herczeg, G. J., Harsono, D., et al. 2019, ApJ, 882, 49
Long, F., Pinilla, P., Herczeg, G. J., et al. 2018, ApJ, 869, 17
Long, M., Romanova, M. M., & Lovelace, R. V. E. 2005, ApJ, 634, 1214
Lopez, B., Lagarde, S., Jaffe, W., et al. 2014, Msngr, 157, 5
Lucy, L. B. 1999, A&A, 344, 282
Luhman, K. L. 2018, AJ, 156, 271
Mannings, V., & Emerson, J. P. 1994, MNRAS, 267, 361
Marsh, K. A., & Mahoney, M. J. 1992, ApJL, 395, L115

McClure, M. K., D'Alessio, P., Calvet, N., et al. 2013, ApJ, 775, 114
Mendigutía, I., Calvet, N., Montesinos, B., et al. 2011, A&A, 535, A99
Mendoza, V. E. E. 1968, ApJ, 151, 977
Millan-Gabet, R., Schloerb, F. P., Traub, W. A., et al. 1999, ApJL, 513, L131
Monnier, J. D., Berger, J.-P., Millan-Gabet, R., et al. 2006, ApJ, 647, 444
Monnier, J. D., & Millan-Gabet, R. 2002, ApJ, 579, 694
Monnier, J. D., Millan-Gabet, R., Billmeier, R., et al. 2005, ApJ, 624, 832
Moshir, M., Copan, G., Conrow, T., et al. 1990, IRAS Faint Source Catalogue, version 2.0 (1990)
Pauls, T. A., Young, J. S., Cotton, W. D., & Monnier, J. D. 2005, PASP, 117, 1255
Petrov, P. P., Grankin, K. N., Gameiro, J. F., et al. 2019, MNRAS, 483, 132
Pinilla, P., Tazzari, M., Pascucci, I., et al. 2018, ApJ, 859, 32
Pollack, J. B., Hollenbach, D., Beckwith, S., et al. 1994, ApJ, 421, 615
Robitaille, T. P., Whitney, B. A., Indebetouw, R., & Wood, K. 2007, ApJS, 169, 328
Schegerer, A. A., Wolf, S., Ratzka, T., & Leinert, C. 2008, A&A, 478, 779
Setterholm, B. R., Monnier, J. D., Davies, C. L., et al. 2018, ApJ, 869, 164
Shakura, N. I., & Sunyaev, R. A. 1973, A&A, 24, 337
St-Onge, G., & Bastien, P. 2008, ApJ, 674, 1032
STScI Development Team 2013, pysynphot: Synthetic Photometry Software Package, version 0.9.12, Astrophysics Source Code Library, ascl:1303.023
Takami, M., Karr, J. L., Hashimoto, J., et al. 2013, ApJ, 772, 145
Tannirkulam, A., Harries, T. J., & Monnier, J. D. 2007, ApJ, 661, 374
Tannirkulam, A., Monnier, J. D., Harries, T. J., et al. 2008, ApJ, 689, 513
ten Brummelaar, T. A., McAlister, H. A., Ridgway, S. T., et al. 2005, ApJ, 628, 453
ten Brummelaar, T. A., Sturmann, J., McAlister, H. A., et al. 2012, Proc. SPIE, 8445, 84453C
ten Brummelaar, T. A., Sturmann, J., Ridgway, S. T., et al. 2013, JAI, 2, 1340004
Tuthill, P. G., Monnier, J. D., & Danchi, W. C. 2001, Natur, 409, 1012
van der Marel, N., Verhaar, B. W., van Terwisga, S., et al. 2016, A&A, 592, A126
VanDerWalt, S., Colbert, S. C., & Varoquaux, G. 2011, CSE, 13, 22
Zajtseva, G. V. 2010, Ap, 53, 212